remote sensing

Article

Frequency Extraction of Global Constant Frequency Electromagnetic Disturbances from Electric Field VLF Data on CSES

Ying Han [1], Qiao Wang [2,*], Jianping Huang [2], Jing Yuan [1], Zhong Li [1], Yali Wang [1], Haijun Liu [1] and Xuhui Shen [3]

1 Institute of Disaster Prevention, Sanhe 065421, China; hanying@cidp.edu.cn (Y.H.)
2 National Institute of Natural Hazards, Ministry of Emergency Management of China, Beijing 100085, China; jianpinghuang@ninhm.ac.cn
3 National Space Science Center, Chinese Academy of Sciences, Beijing 100085, China
* Correspondence: qiaowang@ninhm.ac.cn

Abstract: The electromagnetic data observed with the CSES (China Seismo-Electromagnetic Satellite, also known as Zhangheng-1 satellite) contain numerous spatial disturbances. These disturbances exhibit various shapes on the spectrogram, and constant frequency electromagnetic disturbances (CFEDs), such as artificially transmitted very-low-frequency (VLF) radio waves, power line harmonics, and interference from the satellite platform itself, appear as horizontal lines. To exploit this feature, we proposed an algorithm based on computer vision technology that automatically recognizes these lines on the spectrogram and extracts the frequencies from the CFEDs. First, the VLF waveform data collected with the CSES electric field detector (EFD) are converted into a time–frequency spectrogram using short-time Fourier Transform (STFT). Next, the CFED automatic recognition algorithm is used to identify horizontal lines on the spectrogram. The third step is to determine the line frequency range based on the proportional relationship between the frequency domain of the satellite's VLF and the height of the time–frequency spectrogram. Finally, we used the CSES power spectrogram to confirm the presence of CFEDs in the line frequency range and extract their true frequencies. We statistically analyzed 1034 orbit time–frequency spectrograms and power spectrograms from 8 periods (5 days per period) and identified approximately 200 CFEDs. Among them, two CFEDs with strong signals persisted throughout an entire orbit. This study establishes a foundation for detecting anomalies due to artificial sources, particularly in the study of short-term strong earthquake prediction. Additionally, it contributes to research on other aspects of spatial electromagnetic interference and the suppression and cleaning of electromagnetic waves.

Keywords: CSES; constant frequency electromagnetic disturbances (CFEDs); spectrogram; automatic recognition of horizontal line; frequency extraction

check for updates

Citation: Han, Y.; Wang, Q.; Huang, J.; Yuan, J.; Li, Z.; Wang, Y.; Liu, H.; Shen, X. Frequency Extraction of Global Constant Frequency Electromagnetic Disturbances from Electric Field VLF Data on CSES. *Remote Sens.* **2023**, *15*, 2057. https://doi.org/10.3390/rs15082057

Academic Editor: David Gomez-Ortiz

Received: 24 February 2023
Revised: 4 April 2023
Accepted: 11 April 2023
Published: 13 April 2023

1. Introduction

Previous studies have demonstrated that during super-large earthquakes and shallow earthquakes, the energy of very-low-frequency (VLF) and ultra-low-frequency (ULF) electromagnetic waves increases, leading to ionospheric disturbances in space. These disturbances are considered to be useful for short-term strong earthquake prediction [1,2]. VLF/LF electromagnetic signals emitted by specific transmitters can propagate in the lower ionosphere, which has become a method for detecting the ionosphere [3]. As a result, scientists have deployed several artificial, ground-based VLF transmitters around the world to continuously transmit VLF electromagnetic waves at different frequencies into space. These signals can propagate upward through the ionosphere, reflect back to the ground, and be received by satellites and ground receiving stations [4].

Low energy loss and long transmission distance are the main characteristics of the VLF electromagnetic wave emitted from the artificial source transmitting station. They can propagate between the earth and the ionospheric waveguide system over long distances and have a significant wave–particle interaction effect [1,5–7]. When a satellite passes over the artificial source transmitter, it can receive the artificial source signal within a specific stable frequency range [8]. However, when the electromagnetic wave propagates to the ionosphere, many parameters will change, including velocity and phase as well as refraction and scattering effects. Therefore, various electromagnetic responses excited by the artificial source VLF signal in the ionosphere have different spatial and temporal characteristics [9].

There are more than 40 artificial-source VLF and LF radio wave transmitters in the world, which are widely used in long-distance navigation, maritime navigation, underwater communication navigation, and ionospheric disturbance detection [10]. During VLF/LF radio wave propagation, when the lower ionosphere above the propagation path is disturbed by various factors, such as solar flares, magnetic storms, lightning discharges, earthquakes, etc., it will cause an abnormal VLF/LF artificial source.

Currently, observations of VLF/LF artificial source signals are conducted using ground-based detection and space-based methods. Since the 1950s, Stanford University has used extremely low-frequency (ELF) and VLF receivers to study the phenomenon of sky electricity, with their AWESOME receivers installed and utilized in various locations across the country [11–13]. The UK Radio Astronomy Association (2021) also uses a VLF receiver to measure sudden ionospheric disturbance caused by solar scintillation, with the frequency band observed being 12–35 KHz. Japan's OMNIPAL narrowband receiver is designed to receive signals from VLF artificial sources around the world and is generally equipped with a vertical electric field antenna and two horizontal magnetic ring antennas for detecting horizontal magnetic fields and vertical electric field signals. Since 2000, Japan, Russia, Greece, Italy, and other countries have carried out joint observations of artificial source waves, primarily using OMNIPAL receivers, with stations mainly based on vertical electric extension antennas [14].

With the development of satellite detection technology, electromagnetic field detection has become the main scientific objective for satellite detection of ionospheric environments. The artificial VLF/LF signal from the ground is typically identified with the broadband electromagnetic detector, with equipment based on probe potential detection and inductive magnetometers. As a result of the large number of VLF/LF artificial transmitters located around the world on the ground, satellites can record the information at each station as a mobile space receiving station, which provides a good platform for studying the anomaly detection of VLF/LF artificial source signals detected by satellites, including seismic detection applications.

Currently, the signal-to-interference-to-noise ratio (SNR) method for satellite VLF radio wave signal detection is used to obtain earthquake-related disturbances. It has been discovered that the SNR of the VLF radio wave signal will decrease significantly before the earthquake, with abnormal recovery after the earthquake and similar variation in multiple stations [15–21]. Additionally, the amplitude method for satellite VLF wave signal detection will also show a significant decrease or increase in the amplitude of the VLF wave signal before the earthquake [19–23]. The simultaneous disturbance observation of the satellite and the foundation can be comparatively analyzed and mutually tested, thereby improving the reliability of the seismic anomaly disturbance [24].

Electromagnetic satellite monitoring of earthquakes began in the 1980s and has since detected a large amount of electromagnetic anomaly information, including solar magnetic storms, substorms, lightning, atmosphere, tides, artificial very-low-frequency transmitters, power systems, and satellite platforms themselves [25–31]. In order to study the temporal and spatial variation in artificial source VLF radio wave signals before earthquakes, it is necessary to automatically analyze and extract the frequency and space–time range of electromagnetic waves emitted by these artificial sources with known or unknown frequencies from these massive satellite data. In a recent article [32], a radio frequency interference detection and localization method was proposed based on a ground range detected image generation mechanism and dual polarization using ground range detected. However, this method may not work for some particular situations. Different spatial electromagnetic disturbances appear in different forms on the spectrogram. For instance, artificial VLF transmitter stations, power systems, and satellite platform disturbances cause changes in the spatial physical environment, presenting as a horizontal line feature above the background intensity on the spectrogram [33]. Based on this horizontal line feature, computer vision technology can be used to automatically recognize horizontal lines on the spectrogram and extract the frequency of CFEDs that produce these lines.

Currently, there are three main methods for automatic recognition of CFEDs on the spectrogram: Hough transform methods [34], density statistics-based methods [35], and K-means clustering methods [36]. While the Hough method can recognize line segments in different directions, it is necessary to find and merge horizontal line segments, making it relatively inefficient. The density statistics method uses a horizontal convolution kernel to enhance the horizontal features, which requires setting a density threshold. However, different density thresholds may lead to varying results for different time–frequency spectrograms, reducing the robustness. The K-means clustering method improves upon the density statistics method by offering strong robustness. It can automatically recognize all clearly visible horizontal lines on the spectrogram, with a missed recognition rate of 0. Therefore, we have chosen to utilize the K-means clustering method to automatically recognize horizontal lines on the spectrogram and extract the frequency of CFEDs that generate these horizontal lines worldwide. This lays a solid foundation for studying spatial electromagnetic disturbance anomaly monitoring, especially for short-term earthquake prediction.

2. Data Collection

In February 2018, CSES was successfully launched. Since then, CSES has been observed in orbit for more than 5 years and has generated a vast body of data. The main scientific goal of CSES is to obtain data, such as global electromagnetic field, plasma, and high-energy particle observations, and to provide scientific data services for short-term earthquake prediction and geospatial physics research [37,38]. CSES has an orbital inclination of 97.4° and an orbital return period of 5 days. In one return period, the global spatial resolution of about 500 km can be observed. The satellite orbits the Earth in about 94 min, and most payloads work in the ±65° latitude range. Observation data are stored in ascending and descending orbits, respectively. The spatial resolution of adjacent ascending (or descending) orbits on the same day is approximately 2000 km. Figure 1 is a diagram showing the trajectory of the CSES satellite orbits for one cycle.

CSES carries eight types of scientific payloads [39–43]: an inductive magnetometer, high-precision magnetometer [44], electric field detector (EFD), global satellite navigation system occultation receiver [45], plasma analyzer [46,47], high-energy particle detector [48], Langmuir probe [49], and triple-frequency beacon transmitter [50]. Space electric field detection is completed with the EFD, which can provide basic data for the study of solar–terrestrial space physics, space weather, and the interaction between the ionosphere and the upper atmosphere, magnetosphere, and other related spheres and their effects. It can also provide data application services for seismic observation research [51]. The detection frequency domain is divided into ULF (0–16 Hz), ELF (6 Hz–2.2 kHz), and VLF (1.8–20 kMHz). The sampling rate of VLF is 50 kHz, and a sampling period of 2.048 s, so there are 2048 sampling points in each working period [52]. Experimental data are waveform data and power spectrum data from the Z component of the VLF band collected with the CSES EFD satellite for 2 years. According to the CSES data specification, the EFD VLF data structure is shown in Table 1.

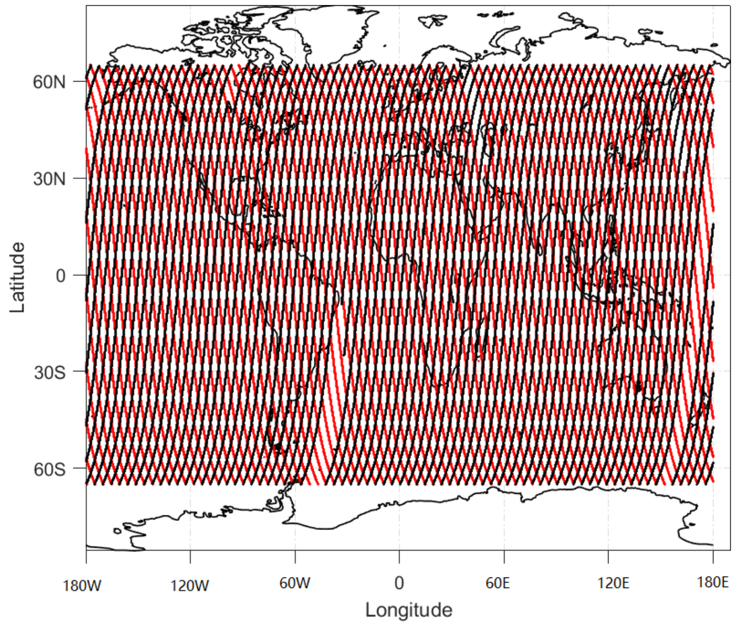

Figure 1. Operation diagram of the CSES satellite in one return period. The red tracks represent the satellite's ascending orbit, and the black tracks represent the descending orbit.

Table 1. EFD VLF level 2 data structure description.

Name	Content	Type	Size	Attribute	Remark
VERSE_TIME	Relative time	64-bit int	N × 1	Unit:ms	
UTC_TIME	Absolute time	64-bit int	N × 1	YYYYMMDD HHMMSSms	
WORKMODE	Workmode	16-bit int	N × 1	1: Inspection 2: Detailed investigation −1: Invalid	
A131_W	X	64-bit float	N × 2048	Unit:mV/m	X component of electric field waveform in WGS84 coordinate system
A132_W	Y	64-bit float	N × 2048	Unit:mV/m	Y component of electric field waveform in WGS84 coordinate system
A133_W	Z	64-bit float	N × 2048	Unit:mV/m	Z component of electric field waveform in WGS84 coordinate system
A131_P	CH1	64-bit float	N × 1024	Unit:mV/m/Hzˆ0.5	Probe ab direction power spectrum
A132_P	CH2	64-bit float	N × 1024	Unit:mV/m/Hzˆ0.5	Probe cd direction power spectrum
A133_P	CH3	64-bit float	N × 1024	Unit:mV/m/Hzˆ0.5	Probe ad direction power spectrum
ALTITUDE	Satellite orbit height	32-bit float	N × 1	Unit:km	The value in WGS84 spherical coordinate system
MAG_LAT	Geomagnetic latitude	32-bit float	N × 1	Unit:degree	
MAG_LON	Geomagnetic longitude	32-bit float	N × 1	Unit:degree	
GEO_LAT	Geographical latitude	32-bit float	N × 1	Unit:degree	The value in WGS84 spherical coordinate system
GEO_LON	Geographical longitude	32-bit float	N × 1	Unit:degree	The value in WGS84 spherical coordinate system
FREQ	Power spectrum frequency	32-bit float	1024 × 1		
FLAG		32-bit int	N × 1		Data quality label

CSES generates 32 orbits per day and uses STFT to convert the waveform data from one orbit into a time–frequency spectrogram. A period (5 days) can generate approximately 130 time–frequency spectrograms. Figure 2 shows a time–frequency spectrogram converted from the Z component of the EFD waveform data from 8 January 2019. The y-axis is the frequency range, the x-axis is the time, longitude, and latitude, and the right color bar is the electromagnetic wave intensity.

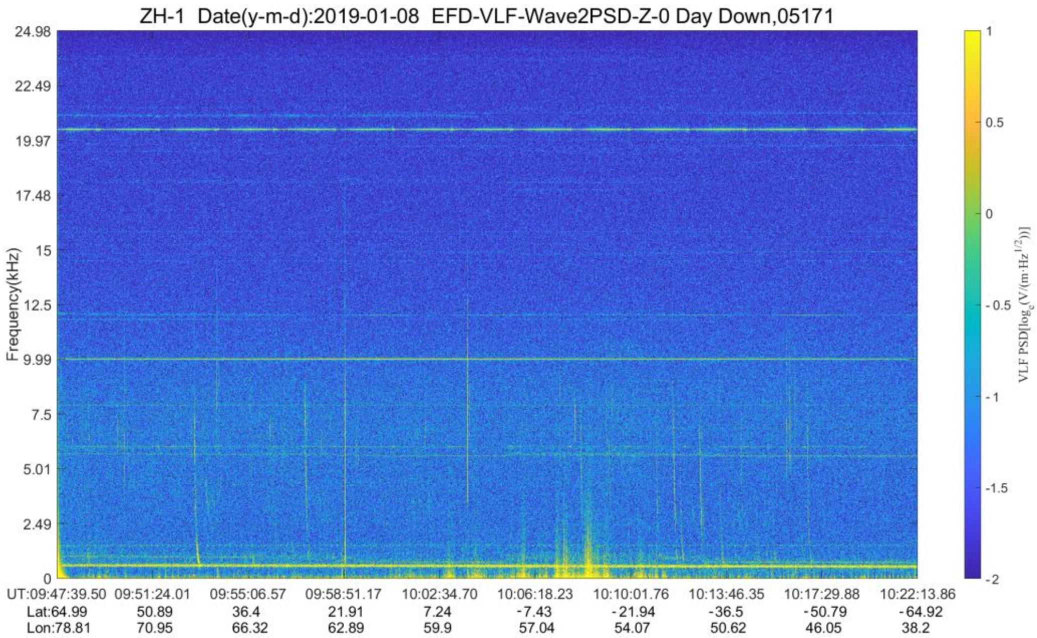

Figure 2. A time–frequency spectrogram of the CSES EFD VLF from 8 January 2019.

3. CFED Recognition Algorithm

3.1. Algorithm Identification Process

The CFED frequency extraction process is shown in Figure 3. First, the EFD VLF waveform data are converted into a time–frequency spectrogram using STFT. Because CFEDs are horizontal lines on the spectrogram, we use the K-means clustering algorithm to cluster each pixel row on the time–frequency spectrogram and merge pixel rows labeled as line clusters into a line after clustering. Then, we calculate the frequency range of each line according to the height ratio between the satellite's VLF frequency domain and the time–frequency spectrogram. Due to the low clarity of the line obtained with the weak CFED signal, or the background enhancement in the time–frequency spectrogram caused by other spatial electromagnetic disturbances, CFED interruptions, etc., these factors will lead to missed recognition of the horizontal line. Therefore, we count a large number of time–frequency spectrograms, determine whether the recognized lines on different time–frequency spectrograms belong to the same CFED, and calculate its frequency range. According to the frequency range, we use the power spectrum data to generate the power spectrogram to verify the CFED and extract its true frequency.

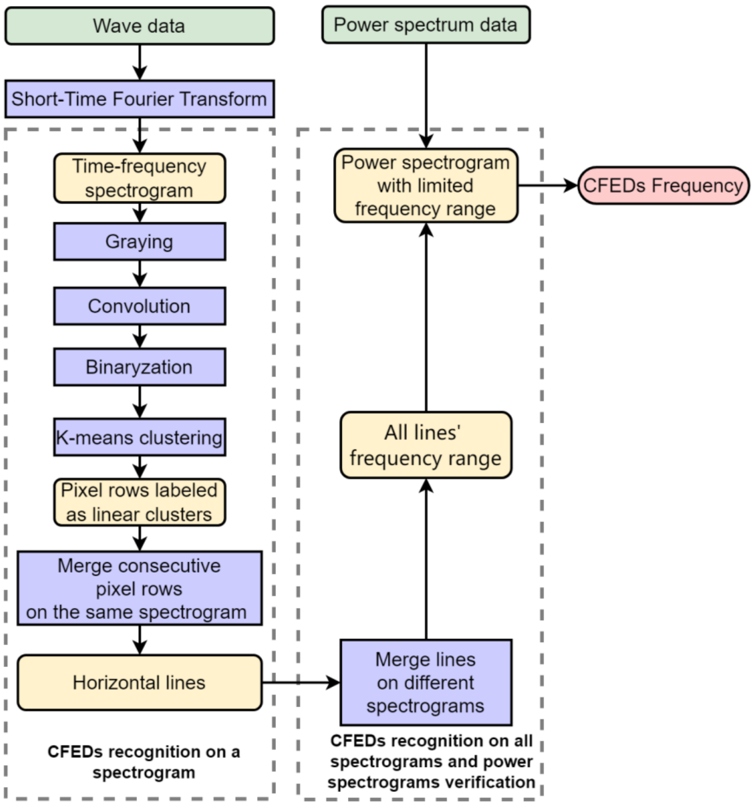

Figure 3. CFED frequency extraction process.

3.1.1. Gray Processing

When using computer vision technology to recognize CFEDs, the basis is that the brightness of the horizontal linear color is higher than the background color on the time–frequency spectrogram, and the horizontal shape is more important than the color. In addition, in order to improve the processing speed of the image, gray processing is used to convert a color time–frequency spectrogram into a grayscale image.

There are many grey processing methods. We obtained the gray spectrogram using the blue channel, i.e., Gray = RGB.B, where RGB is a time–frequency spectrogram and B is the blue channel of a color image [36]. Figure 4a shows a time–frequency spectrogram, and Figure 4b shows a gray image obtained using the blue channel.

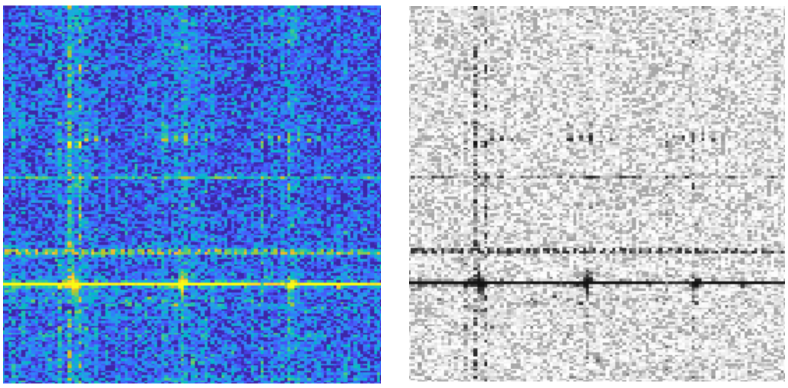

(**a**) (**b**)

Figure 4. Gray processing. (**a**) A time–frequency spectrogram. (**b**) The blue channel of (**a**).

3.1.2. Convolution Operation

Because the horizontal features of the lines on the time–frequency spectrogram are recognized, in order to improve the recognition rate, the horizontal convolution kernel is used to enhance its horizontal features. The horizontal convolution kernel is provided by Equation (1).

$$\text{kernel} = [1, 0, -1] \tag{1}$$

The method is expressed as Equation (2). Figure 5a shows a 5 × 5 pixel spectrogram that is zoomed without distortion. A horizontal line on the map is significantly enhanced after convolution, as shown in Figure 5b. Figure 6 shows the result convolution of Figure 4b.

$$\text{cov\_dst}(x, y) = \sum_{\substack{0 \leq x' < \text{kernel.cols}, \\ 0 \leq y' < \text{kernel.rows}}} \text{kernel}(x', y') \times \text{gray}(x + x' - \text{anchor}.x, y + y' - \text{archor}.y) \tag{2}$$

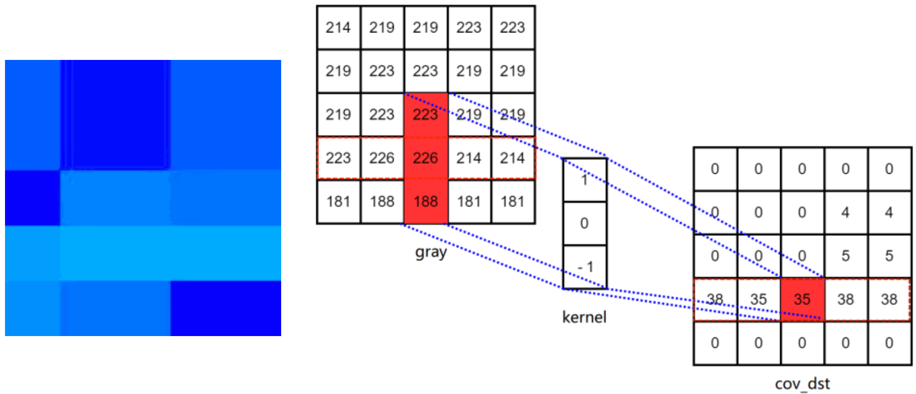

(**a**) (**b**)

Figure 5. Horizontal convolution. (**a**) A 5 × 5 pixel spectrogram zoomed without distortion. (**b**) Horizontal convolution operation. The line shown in Figure 5a is enhanced after convolution.

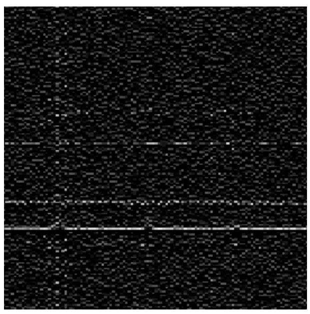

Figure 6. Result after the convolution of Figure 4b.

3.1.3. Binary Processing

In order to reduce the image and increase the algorithm's ability to identify edges and features more accurately, the target image is binarized after convolution. Binary processing is expressed by Equation (3), where *cov_dst* is the gray image after convolution; *i* and *j* are the coordinates of a pixel on cov_dst; max is the maximum number of pixels, which is set to 255; and thresh is the threshold, which is set to 10 on paper. Figure 7 shows the result of the binarization of Figure 6.

$$\text{bi\_map}(i, j) = \begin{cases} max & if\ \text{cov\_dst}(i, j) > tresh \\ 0 & \text{otherwise} \end{cases} \tag{3}$$

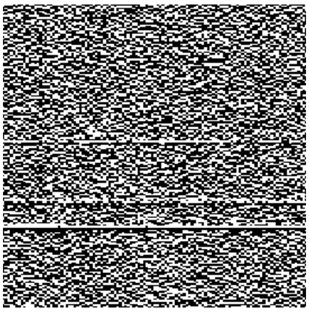

Figure 7. Results after the binarization of Figure 6.

3.1.4. K-Means Clustering

The clustering algorithm, also known as 'unsupervised classification', aims to divide data into meaningful or useful groups (or clusters). In order to recognize the horizontal line on the image, we use the K-means clustering algorithm to cluster the white pixels. K is the number of clusters, and because we only need to separate lines and non-lines, we set $k = 2$.

The steps are as follows:

Step 1: Randomly select k cluster centroid points $\{\mu 1, \mu 2, \ldots, \mu n\}$ ($k = 2$).

Step 2: Repeat the following process until convergence:

(1) For each sample i, calculate the class it should belong to.

$$c^{(i)} := \underset{j}{\operatorname{argmin}} ||x^{(i)} - \mu_j||^2 \tag{4}$$

(2) Calculate each class j and repeat the centroid of the class.

$$\mu_{\mathrm{i}} := \frac{\sum_{i=1}^{m} 1\{c^{(i)} = k\} x^{(i)}}{\sum_{i=1}^{m} 1\{c^{(i)} = j\}} \tag{5}$$

where $c^{(i)}$ denotes the nearest class between the sample i and k classes, and its value is between 1 and k. The centroid μ_j represents a guess for the sample center point belonging to the same clusters.

After clustering, the binarized image is grouped into two clusters. In order to clearly identify the clustering results, linear clusters are marked with red dots. Figure 8 shows the result of clustering Figure 7.

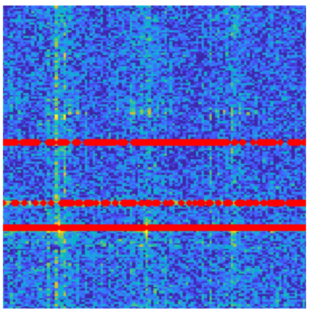

Figure 8. Clustering results of Figure 7. Line clusters are marked with red dots on Figure 4a.

3.2. Extracting CFED Frequency from a Time–Frequency Spectrogram

After K-means clustering, all pixel rows on the binary image are clustered into line and non-line clusters. As shown in Figure 9, Figure 9a is a spectrogram and Figure 9b is its clustering result, and the clearly visible lines in Figure 9a are clustered into line clusters. The horizontal and vertical coordinates in Figure 9b correspond to the width and height of the time–frequency spectrogram 9a, which are *map_width* and *map_height*, respectively.

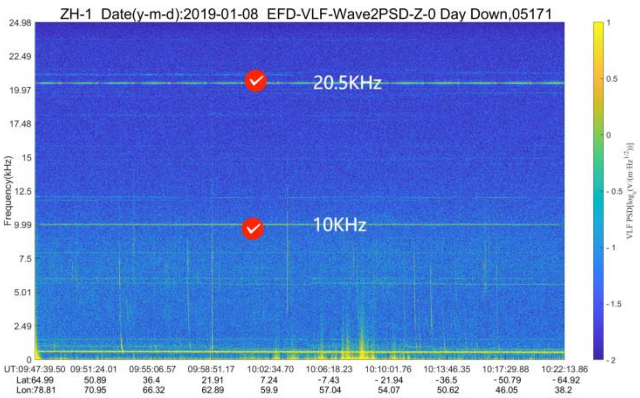

(**a**)

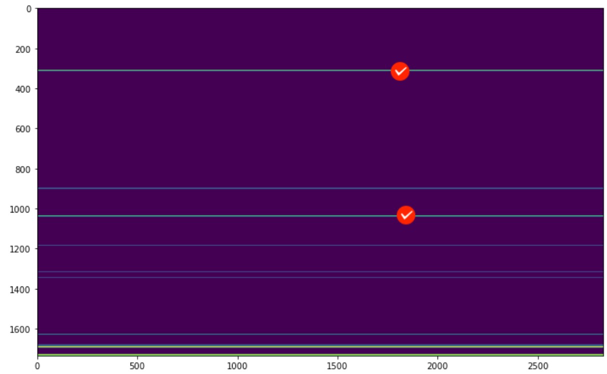

(**b**)

Figure 9. Clustering results. (**a**) Original time–frequency spectrogram. (**b**) K-means clustering results.

The line thickness on the spectrogram differs according to the signal strength and frequency domain of CFED. Some lines are a row of pixels, and the frequency is a value, as shown in Figure 10①, whereas some lines are multiple rows of pixels, as shown in Figure 10②, where the frequency is a range. The recognition algorithm not only recognizes the lines but also calculates the *line_height* on the spectrogram. The frequency corresponding to each line is calculated according to the CSES VLF range. The calculation method is as follows.

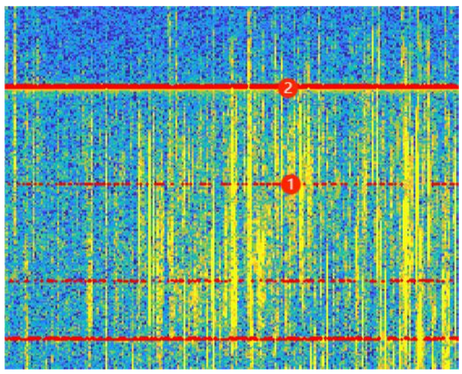

Figure 10. Line recognition result marking.

3.2.1. Extract the Frequency of a Pixel Row

Figure 11 shows the relationship between row height and frequency, where *max_high* is the height of the time–frequency spectrogram; *max_freq* is the maximum frequency, where *max_freq* = 24975.6; and the minimum frequency and minimum height are 0. The recognized line frequency is calculated using Equation (6), where *line_freq* is the pixel row frequency and *line_high* is the pixel row height on the spectrogram.

$$line\_freq = \max\_fre - \frac{max\_freq \times line\_high}{map\_height} \quad (6)$$

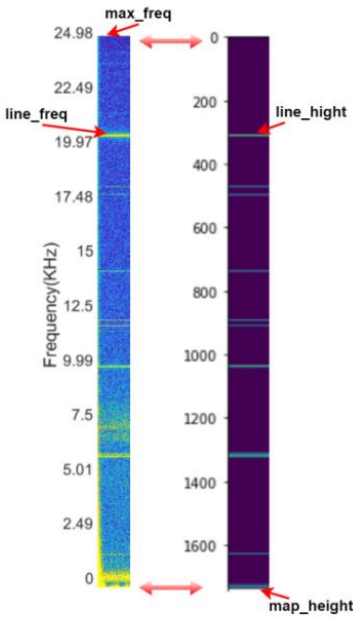

Figure 11. Correspondence between spectrogram and clustering results.

3.2.2. Extract the Frequency Range of a Line Containing Continuous Multi-Pixel Rows

If a thick line consists of continuous multi-pixel rows, then the row heights are (*line_high1, line_high2 . . . Line_highn*), and the corresponding frequencies of each row of pixels are (*line_freq1, line_freq2 . . . line_freqn*). The line frequency range is (*line_freq_min*, *line_freq_max*), where *line_freq_min = line_freq1* and *line_freq_max = line_freqn*.

So, for the linei (i = 1,2 . . .), if it is a single row of pixels, linei_fre=linei_freq; if it is multi-pixel rows, linei_fre= (linei_freq_min, linei_freq_max).

3.2.3. Extract all Horizontal Line Frequency Ranges for a Period (5 days)

Due to other spatial electromagnetic disturbances, the spectrogram background is enhanced, morning and dusk are alternately affected, or the intensity of the transmitted signal of the electromagnetic signal transmitting station changes, all of which will lead to changes in the shape of the line on the spectrogram, as shown in Figure 12①,②, which has a certain impact on the results of line recognition [53]. For example, line clarity is reduced, resulting in missed recognition; the broadening in the signal frequency domain makes the frequency domain range of the identified CFED larger. Therefore, in order to avoid missing CFED recognition, and considering the frequency extraction of CFED globally, it is necessary to recognize and count lines on a large number of spectrograms. When recognized lines are on different spectrograms, it is necessary to determine whether they are the same CFED. For example, Figure 12①–④. The decision method is shown in Figure 13. When line 1 and line 2 satisfy the following seven cases, they can be determined to be the same CFED. *Freq* is the CFED frequency range.

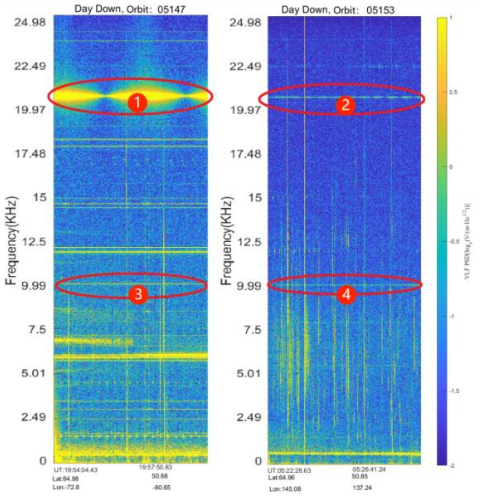

Figure 12. Different forms of the same line on different spectrograms.

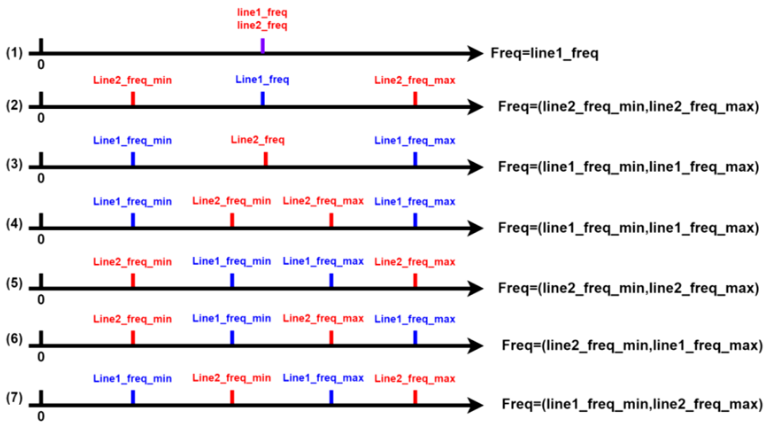

Figure 13. Method to decide whether two lines on different spectrogram belong to the same CFED.

3.2.4. Extract the Frequency Value by Power Spectrogram

The previous extraction is only the frequency range of the CFED, not its true frequency value. Combined with this frequency range, we use the satellite's power spectrogram to extract its true frequency value. The steps are as follows:

Step 1: According to the frequency range, combined with the FREQ file of CSES, as shown in Table 1, find the coordinate range corresponding to the frequency range.

Step 2: According to the coordinate range obtained in step 1, the power spectrum Z component file A133_P is traversed to generate power spectrograms corresponding to the frequency range.

Step 3: Observe the horizontal electromagnetic wave on the power spectrogram, confirm the existence of CFED, and extract the true frequency value.

For example, after a series of calculations, a frequency range *Freq* = (10,117, 10,002) is obtained, and the power spectrogram of the *Freq* range is generated using the power spectrum data, as shown in Figure 14. It can be seen that this CFED is true in the *Freq*, and its frequency is 10 kHz.

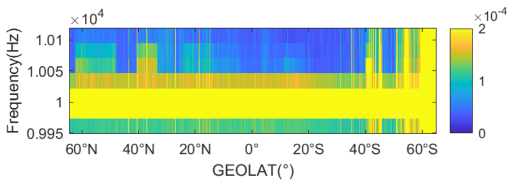

Figure 14. A power spectrogram generated over the frequency range (10,117, 10,002), where y is the frequency, x is the latitude, and the color bar is the signal strength.

4. Experimental Results and Analysis

4.1. Experimental Environment

We use Matlab2020 to generate time–frequency spectrograms and power spectrograms. We use python3.7 to call CV2 and the SKLearn clustering algorithm library to perform CFED recognition.

4.2. Experimental Data

Experimental data were randomly selected from the CSES EFD VLF waveform data and power spectrum data for a total of 8 orbital periods from 2019 and 2020. The data structure is shown in Table 1. The one orbit (ascending or descending) waveform data obtained one time–frequency spectrogram, with a total of 1043 time–frequency spectrograms, as shown in Table 2.

Table 2. Experimental data.

Orbital Period	Start and End Time (YYMMDD-YYMMDD)	Time–Frequency Spectrogram Number
Period 1	20190106-20190110	130
Period 2	20190720-20190724	130
Period 3	20190725-20190729	122
Period 4	20190730-20190804	149
Period 5	20200601-20200605	130
Period 6	20200626-20200630	130
Period 7	20200701-20200705	130
Period 8	20200722-20200726	122
SUM		1043

4.3. Recognize the Horizontal Lines

To recognize the horizontal lines, we traversed each time–frequency spectrogram for a period (5 days), clustered the pixel rows using K-means after preprocessing, and statistically analyzed the recognition results for each period. Table 3 shows the number of horizontal lines for each period.

Table 3. Number of horizontal lines in each period.

Orbital Period	Start and End Time (YYMMDD-YYMMDD)	Numbers of Lines
Period 1	20190106-20190110	1529
Period 2	20190720-20190724	1436
Period 3	20190725-20190729	1463
Period 4	20190730-20190804	1636
Period 5	20200601-20200605	1761
Period 6	20200626-20200630	1821
Period 7	20200701-20200705	1698
Period 8	20200722-20200726	1385

The experimental results show that several spectrograms in each period cannot recognize a horizontal line. A record of the number of orbits that do not recognize a horizontal line is shown in Table 4.

Table 4. Number of spectrograms without a recognized horizontal line.

Orbital Period	Start and End Time (YYMMDD-YYMMDD)	Number of Spectrograms without a Recognized Horizontal Line
Period 1	20190106-20190110	7
Period 2	20190720-20190724	13
Period 3	20190725-20190729	11
Period 4	20190730-20190804	11
Period 5	20200601-20200605	12
Period 6	20200626-20200630	0
Period 7	20200701-20200705	7
Period 8	20200722-20200726	13

4.4. Extract the Frequency Range and Verify CFED Using a Power Spectrogram

The horizontal lines in Table 3 have not been merged before, and there are many inclusions or overlapping relationships between the line frequency ranges. According to the method in Section 3.2.3, we merged all the lines in eight periods. In this study, according to the CSES VLF frequency range (1.8 kHz to 24.98 kHz), more than 200 lines were obtained after merging. Then, for the 200-line frequency range, we used the power spectrogram to verify the CFEDs and extract the true frequency. Table 5 shows the statistical results of the top 10 CFED frequency ranges, appearance times, the power spectrogram of the corresponding frequency range, and the extracted final true frequency.

Table 5. Frequency range and number of top 10 in the 8 periods with the corresponding frequency range power spectrogram.

Ranking	Appearance Times	Frequency Range	True Frequency(kHz)	Corresponding Frequency Range Power Spectrogram
1	947	12,005–12,207	12.1	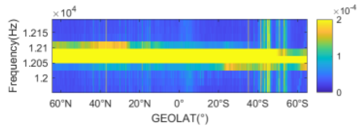
2	913	10,002–10,117	10	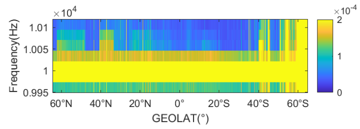
3	913	5851–6183	5.9 and 6	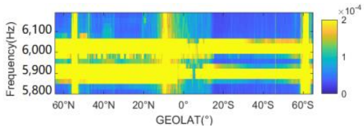
4	722	20,407–20,652	20.5	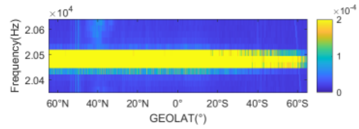
5	637	15,565–15,651	15.6	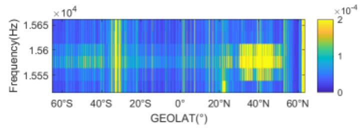
6	575	14,441–14,585	14.5	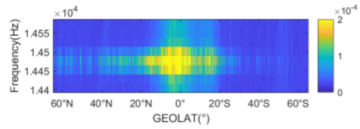
7	478	18,098–18,433	18.2	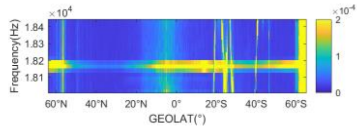
8	475	11,789–11,947	11.8	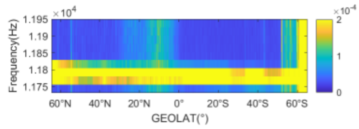

Table 5. *Cont.*

Ranking	Appearance Times	Frequency Range	True Frequency(kHz)	Corresponding Frequency Range Power Spectrogram
9	426	2462–2522	2.46	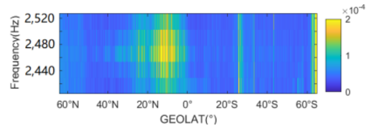
10	426	2998–3055	3	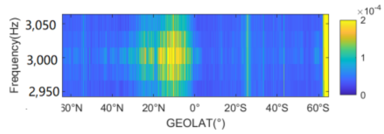

Figure 15 shows the CFED power spectrograms with relatively stable and strong signals except for the top 10.

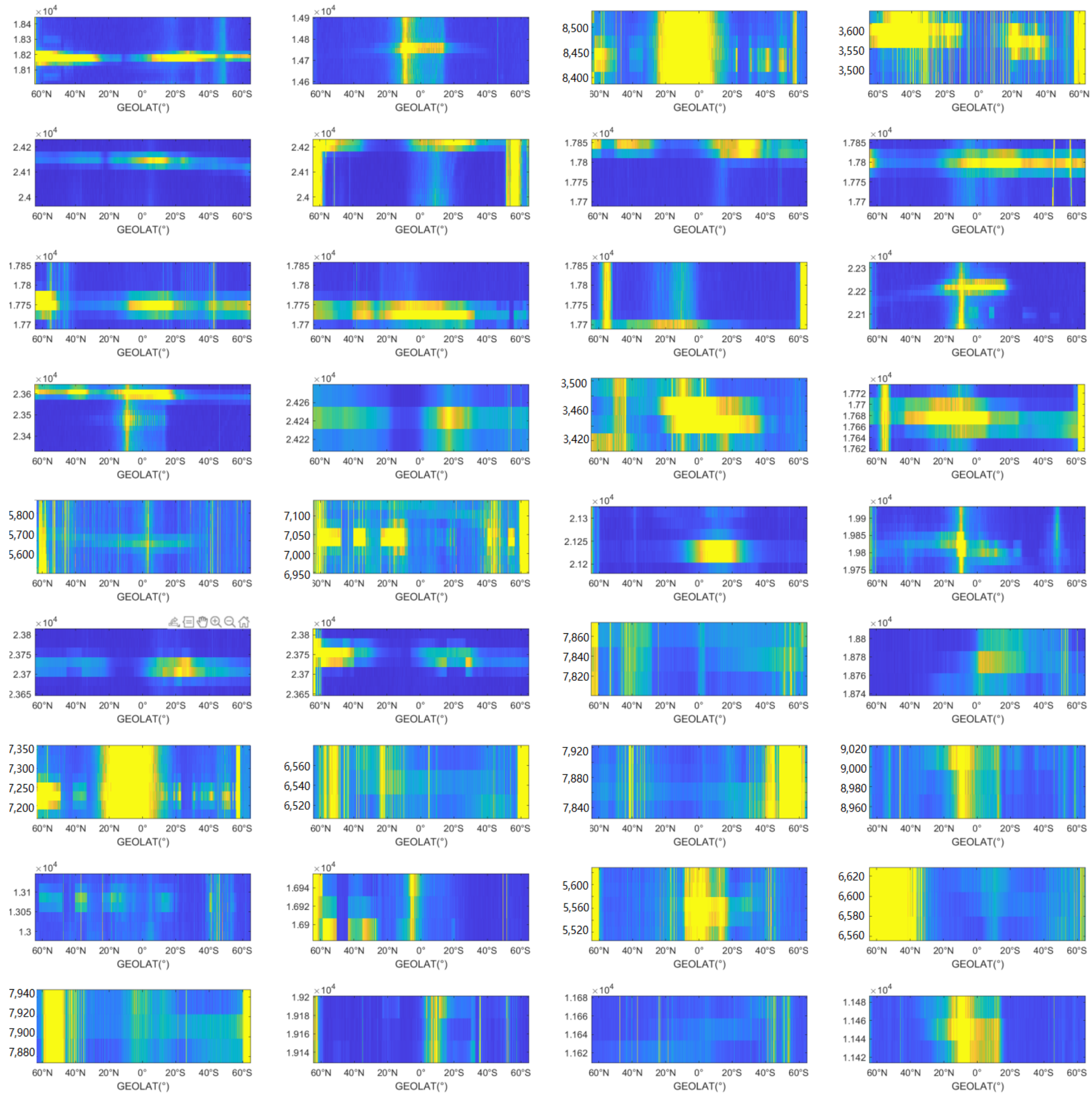

Figure 15. Other recognized partial CFED power spectrograms after ranking the top 10.

4.5. Results Analysis

4.5.1. Reasons for the Low Occurrence of CFED Statistical Results

The probability of CFED being recognized depends primarily on the signal strength and spatial domain range. The weaker the signal, the lower the line clarity on the time–frequency spectrogram, and the easier it is to miss recognition. Once disturbed by other electromagnetic waves, the missed recognition rate is increased. Although some of the signal strength is large, the spatial domain is small, and the signal can only be captured by the EFD of some orbits, and the number of times recognized is also small.

4.5.2. A Few Frequency Ranges Are Wide after Merging

Because the lines are too close, if they are disturbed by other electromagnetic waves, the frequency range becomes wider and the closer lines on the spectrogram are merged into one line. We corrected these issues when using the power spectrogram to verify the existence of CFED. For example, as shown in Figures 16 and 17, different frequencies are merged into a frequency range. Figure 16 shows frequencies merged into a frequency range, and this error is found and corrected into two CFEDs when verified using the power spectrogram. At the same time, we found an interesting phenomenon that they either appear or disappear at the same time in the power spectrogram.

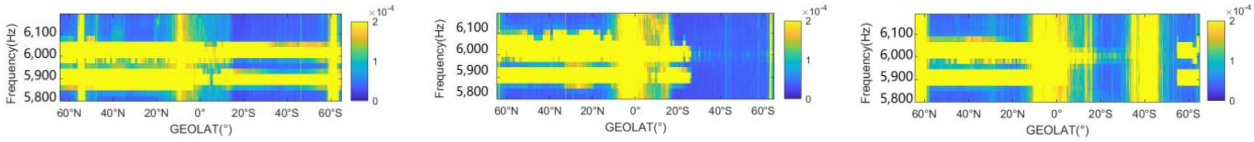

Figure 16. Two CFEDs in a frequency domain (5851–6183). On power spectrograms, they appear or disappear at the same time.

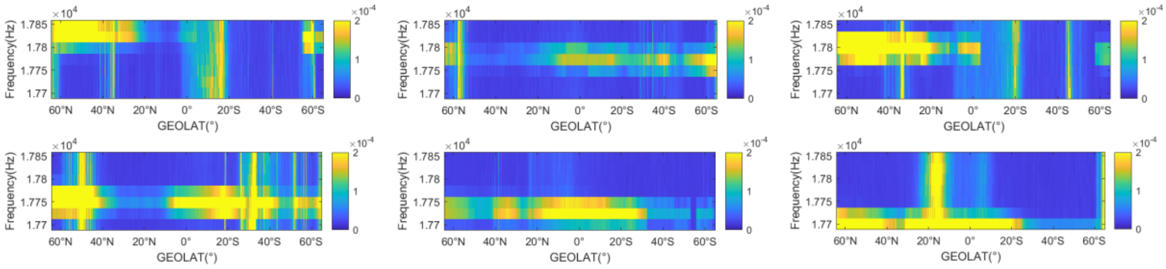

Figure 17. Six CFEDs merged in one frequency range (17741-17856), which never appear in the same spectrogram at the same time.

Figure 17 also shows a group of CFEDs within a frequency range (17,741–17,856), ranking seventh in statistics with 475 occurrences. It contains six CFEDs with high signal strength. We also found an interesting phenomenon that in the existing eight-period power spectrograms, they never appear in the same spectrogram at the same time, as shown in Figure 18.

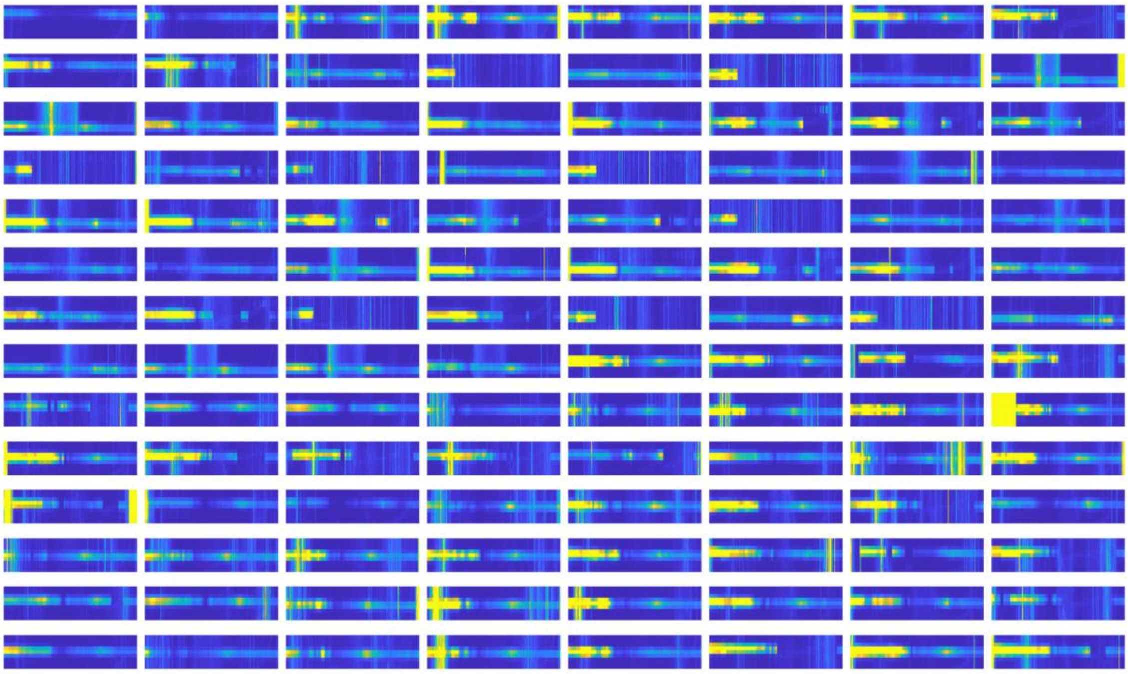

Figure 18. Six CFEDs that never appear on the same power spectrogram at the same time and seem to be alternately emitting signals.

4.5.3. CFEDs That Exist throughout the Period

In the process of experimental statistics, we found that there are two CFEDs with strong signals on CSES, and their frequencies are 10 kHz and 20.5 kHz, respectively, as shown in Figure 9a. The existence of its full period is verified with the power spectrogram, as shown in Figures 19 and 20. There are also other full-period electromagnetic wave disturbances, but their weak signals often lead to missed recognition.

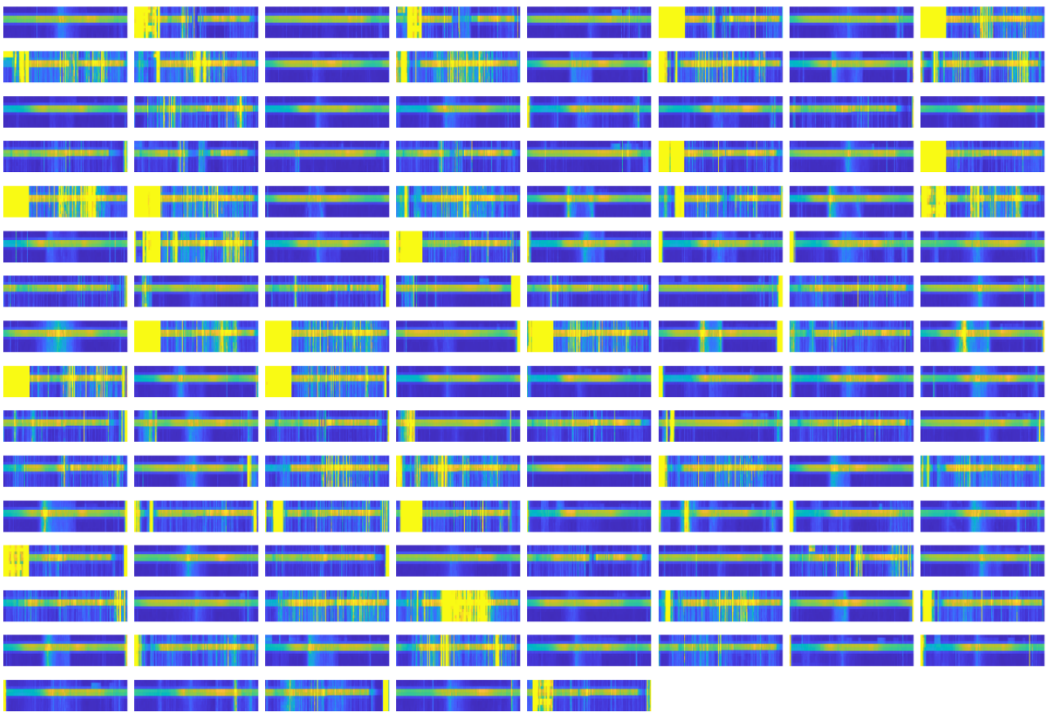

Figure 19. Power spectrograms of 125 10kHz CFEDs from one period. The signal is stable.

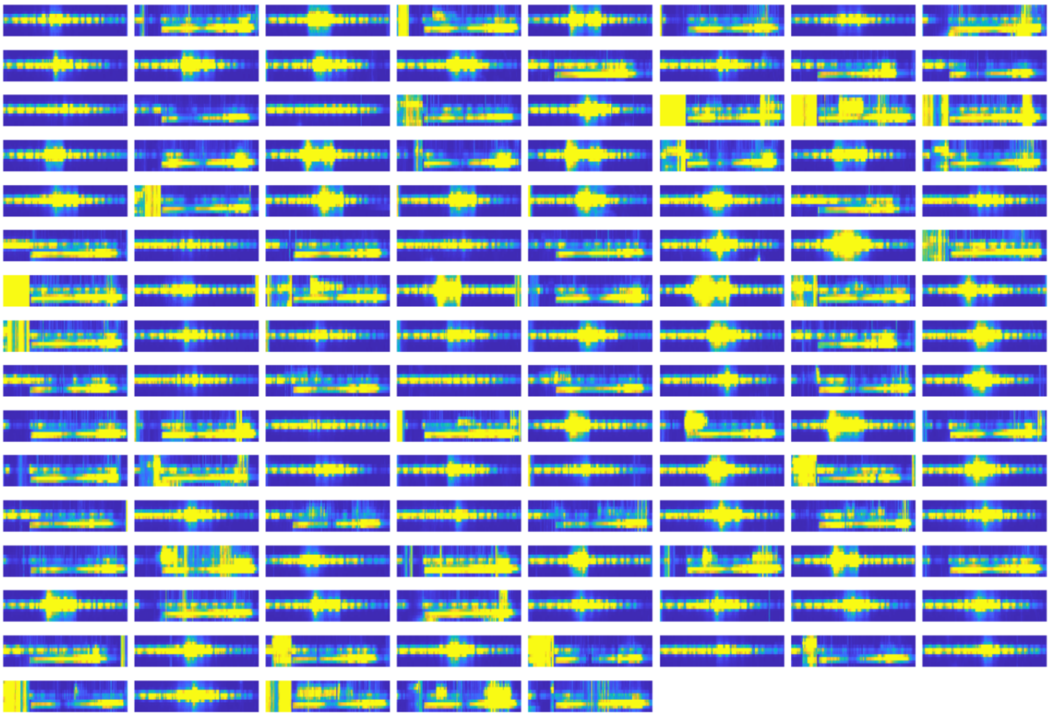

Figure 20. 125 power spectrograms of 20.5 kHz CFEDs from one period. The signal is not stable.

However, whether on the time–frequency spectrogram or on the power spectrogram, the signal strength and frequency of the electromagnetic wave at 10 kHz are very stable, while the signal at 20.5 kHz is unstable, which changes greatly with time and signal strength, as shown in Figures 19–21.

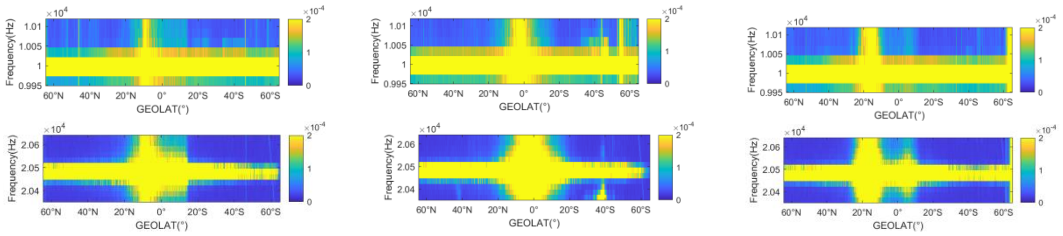

(**a**) (**b**) (**c**)

Figure 21. Comparison of 10 kHz CFED and 20.5 kHz CFED power spectrogram from the same orbit data. (**a**) Orbit:051350; (**b**) Orbit:051430; and (**c**) Orbit:051490.

This 10 KHz CFED hardly changes with the time domain. This strong signal characteristic of the frequency domain stability and global existence is of great significance for studying other electromagnetic disturbances.

5. Discussion

Using experiments on CSES EDF VLF over eight orbital periods, we found about 200 CFEDs and extracted their frequencies. We also found that 10 kHz CFED and 20.5 kHz CFED exist during the full orbital period. Based on the existing findings, we can find and explore more meaningful applications.

5.1. Frequency Value and CFED Localization Problem

For a verified CFED, whether it should be represented with a frequency point or frequency domain remains to be further studied. For example, should the frequency be 20.5 kHz or (20.45 kHz–20.51 kHz), as shown in Figure 22?

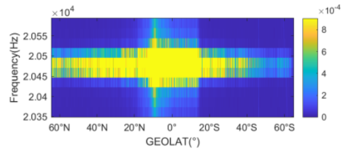

Figure 22. Power spectrogram of a CFED.

Another problem to be solved is locating the CFED launch point and transmission coverage range. The article provides a tool for monitoring radio frequency interference [32]. Future research can use this method to solve CFED launch location.

5.2. Verification of CFED and the Extraction Frequency Method

Currently, when checking CFED, manual verification is used. This method is accurate, but the workload is relatively large for large amounts of data. The next step is to consider automatic verification using computer vision technology, but the signal strength of some CFEDs is weak. On the power spectrogram, the signal strength is looming, as shown in Figure 23, which is also a very big challenge for computer vision.

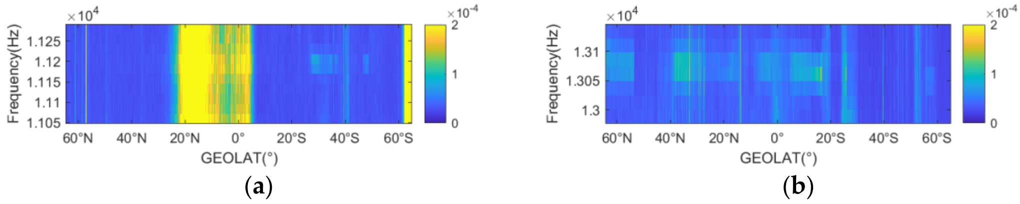

Figure 23. CFEDs with weak signal strength on the power spectrogram. (**a**) 11.2 kHz; (**b**) 13.05 kHz.

5.3. Time–Frequency Spectrogram Orbit Data without Line Recognition

Since the power spectrogram has verified the existence of 10kHz and 20.5 kHz CFEDs over the entire period (5 days), why are some lines not recognized on some time–frequency spectrograms? As shown in Table 4, after observing time–frequency spectrograms, we found that these spectrograms were disturbed by other space electromagnetic waves, resulting in an enhanced background, so no lines were recognized. Usually, CFEDs are clearly visible on the time–frequency spectrogram without strong interference from other electromagnetic waves and can be easily recognized, as shown in Figure 24, where red represents the result marker of the recognized line. When subjected to other electromagnetic disturbances, the background field in the time–frequency spectrogram is enhanced or the electromagnetic wave is coupled, so the straight line is looming on the time–frequency spectrogram, resulting in missed detection, as shown in Figure 25.

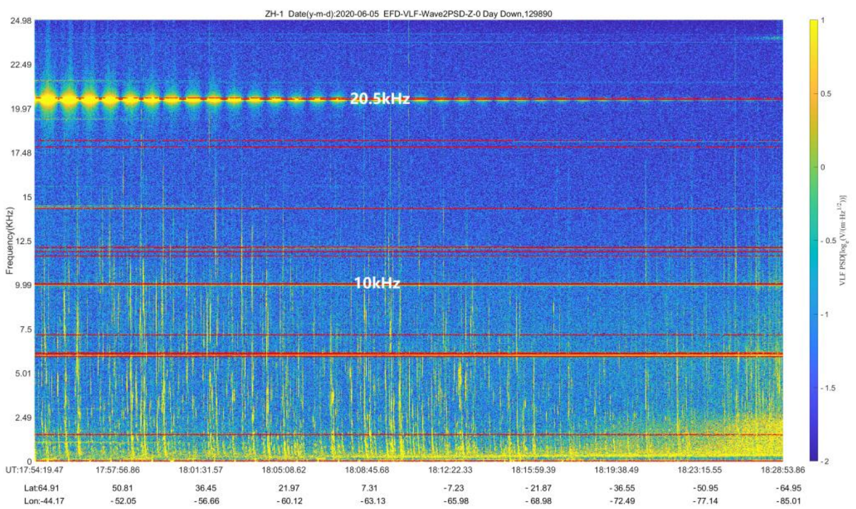

Figure 24. CFEDs marking on a time–frequency spectrogram with less spatial disturbance.

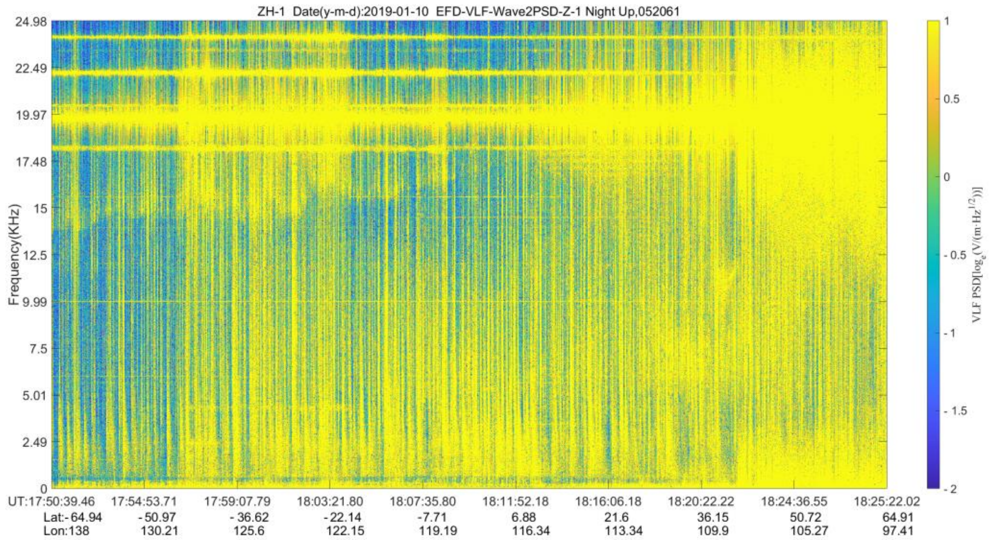

Figure 25. No CFED is recognized due to interference from other space electromagnetic waves.

We plotted the trajectory based on undetected CFED orbits in Table 4, as shown in Figure 26. It can be seen from the figure that most of these tracks are concentrated in the ellipse-marked area in Figure 26. The reasons for this result need to be further explored using an expanded data set.

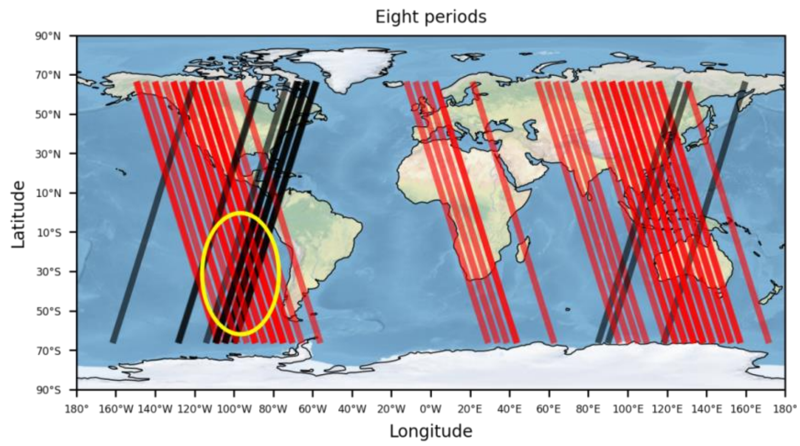

Figure 26. Trajectory diagram of undetected CFEDs. The red trajectory line is the satellite's ascending orbit, and the black trajectory line is the satellite's descending orbit. The darker the color, the more the trajectory overlaps. The yellow elliptical region has the highest number of undetectable signal occurrences.

5.4. Other Space Electromagnetic Wave Disturbance Anomaly Detection

The 10kHz CFED hardly changes with the time domain. This strong signal characteristic of frequency stability and global existence is of great significance for studying other electromagnetic disturbances. When this 10 kHz CFED cannot be recognized, it indicates that this orbit is disturbed by other electromagnetic waves in space, as shown in Figure 27. When the 10kHz CFED can be recognized, but the density of the line breaks or becomes sparse, it can also be determined that the position is disturbed by other space electromagnetic waves, as shown in Figure 28. This detection of other electromagnetic disturbances in space is much more efficient than that of the paper [53].

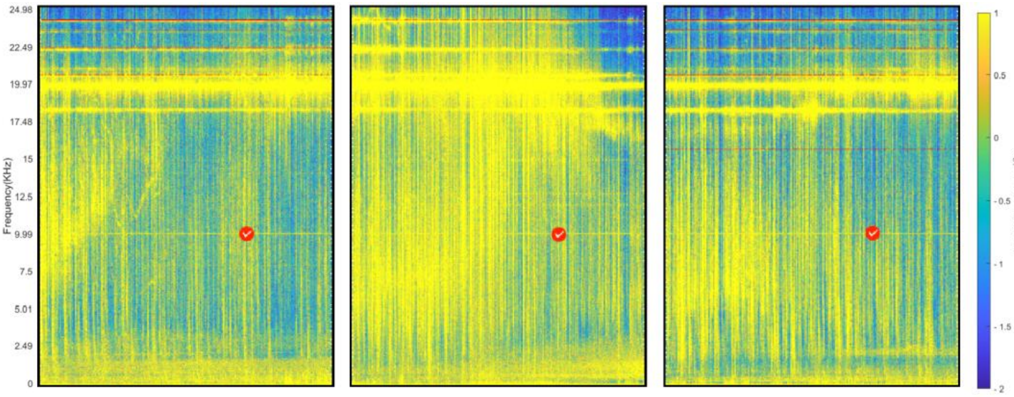

Figure 27. The time–frequency spectrogram of 10kHz CFED cannot be detected.

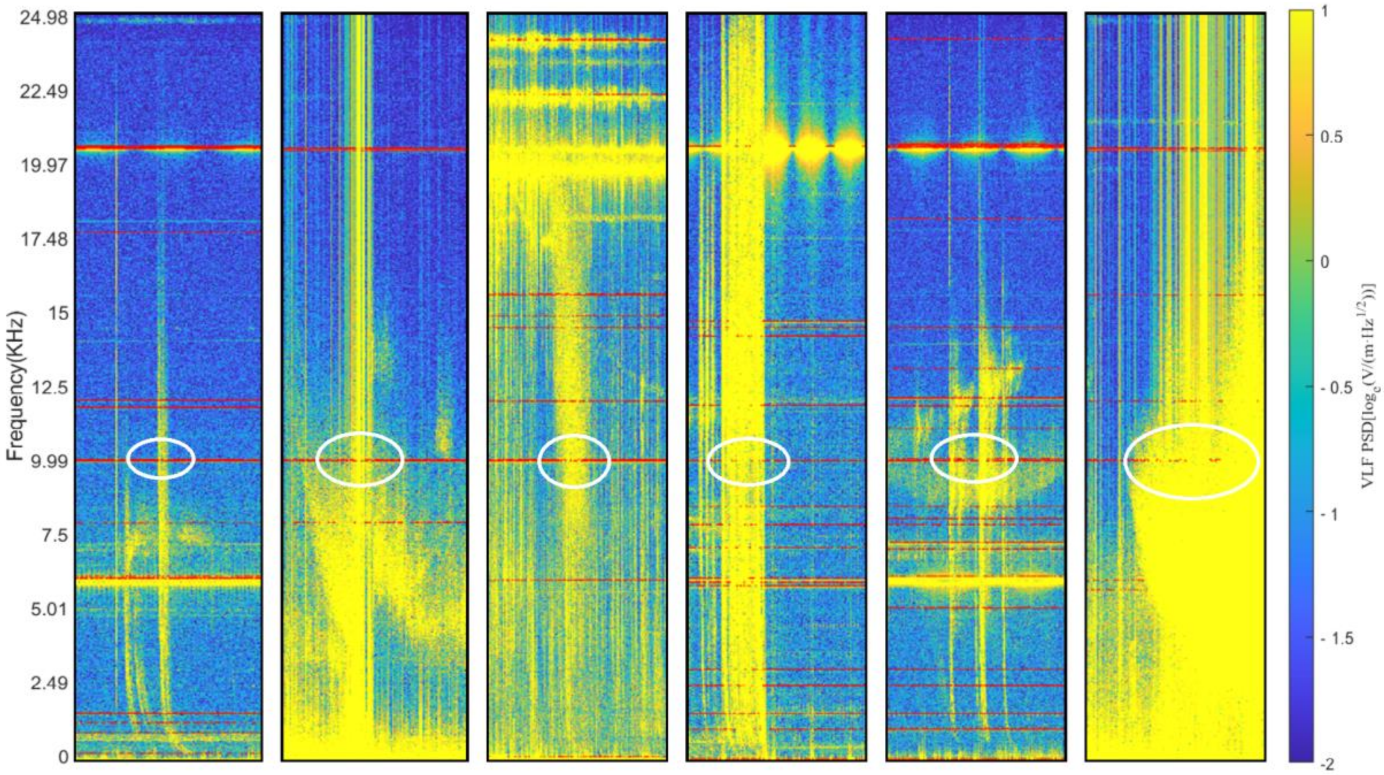

Figure 28. When the 10 kHz CFED is interfered by other electromagnetic waves, there is a change in linear density, as shown in the white oval in the picture.

6. Conclusions

Regarding the CFED horizontal lines on the spectrogram, we utilized computer vision technology to identify and extract the frequency range of these horizontal lines on the time–frequency spectrogram. We then used power spectrogram data to verify CFED in this frequency range and extract the actual frequency values. We collected a total of 1043 orbit data from 8 periods of CSES EFD VLF. Using experimental statistics and analysis, we were able to extract more than 200 CFEDs, and found 2 CFEDs with a complete cycle and strong signal at 10 kHz and 20.5 kHz. These results are of great research significance for the detection of other spatial electromagnetic disturbances and provide a foundation for suppressing waveforms to achieve waveform data cleaning.

Moving forward, our focus will be on two main aspects: extracting the spatial parameters of the CFEDs and suppressing the CFEDs to clean the waveform data.

Author Contributions: Conceptualization, methodology, writing—original draft, and writing—review and editing, Y.H.; methodology, funding acquisition, and writing—review and editing, Q.W.; methodology, J.Y.; data curation, J.H.; supervision, X.S.; and investigation, resources, and software, Z.L., Y.W. and H.L. All authors have read and agreed to the published version of the manuscript.

Funding: This research was funded by the NSFC project (grant no. 42104159), China Earthquake Administration Teacher Research Fund Project (grant no.20150109), and the Fundamental Research Funds for the Central Universities (grant no. ZY20215143).

Data Availability Statement: Publicly available datasets were analyzed in this study. The CSES electric field data can be found here: (www.leos.ac.cn, accessed on 1 September 2021).

Acknowledgments: This work used the data from the CSES mission, a project funded by the China National Space Administration (CNSA) and the China Earthquake Administration (CEA). Thanks to the CSES team for the data (www.leos.ac.cn, accessed on 1 September 2022).

Conflicts of Interest: The authors declare no conflict of interest.

References

1. Xiong, P.; Long, C.; Zhou, H.; Battiston, R.; Zhang, X.; Shen, X. Identification of Electromagnetic Pre-Earthquake Perturbations from the DEMETER Data by Machine Learning. *Remote Sens.* **2020**, *12*, 3643. [CrossRef]
2. Ni, B.; Bortnik, J.; Thorne, R.M.; Ma, Q.; Chen, L. Resonant scattering and resultant pitch angle evolution of relativistic electrons by plasmaspheric hiss. *J. Geophys. Res. Space Phys.* **2013**, *118*, 7740–7751. [CrossRef]
3. Ni, B.; Huang, H.; Zhang, W.; Gu, X.; Zhao, H.; Li, X.; Cao, X. Parametric sensitivity of the formation of reversed electron energy spectrum caused by plasmaspheric hiss. *Geophys. Res. Lett.* **2019**, *46*, 4134–4143. [CrossRef]
4. Zhang, X.M.; Qian, J.D.; Shen, X.H.; Liu, J.; Wang, Y.L.; Huang, J.P.; Ouyang, X.Y. The seismic application progress in electromagnetic satellite and future development. *Earthquake* **2020**, *40*, 18–37.
5. Otirakis, S.M.; Asano, T.; Hayakawa, M. Criticality analysis of the lower ionosphere perturbations prior to the 2016 Kumamoto (Japan) earthquakes as based on VLF electromagnetic wave propagation data observed at multiple stations. *Entropy* **2018**, *20*, 199. [CrossRef]
6. Singh, V.; Hobara, Y. Simultaneous study of VLF/ULF anomalies associated with earthquakes in Japan. *Open J. Earthq. Res.* **2020**, *9*, 201–215. [CrossRef]
7. Wang, S.; Gu, X.; Luo, F.; Peng, R.; Chen, H.; Li, G.; Yuan, D. Observations and analyses of the sunrise effect for NWC VLF transmitter signals. *Chin. J. Geophys.* **2020**, *63*, 4300–4311.
8. Zhao, G.Z.; Lu, J.X. Monitoring and analysis of earthquake phenomena by artificial SLF Waves. *Eng. Sci.* **2003**, *5*, 27–32.
9. Zhao, S.; Liao, L.; Zhang, X.; Shen, X. Full wave calculation of ground-based VLF radiation penetrating into the ionosphere. *Chin. J. Radio Sci.* **2016**, *31*, 825–833.
10. Loudet, L. SID Monitoring Station[EB/OL]. 2013. Available online: https://sidstation.loudet.org/stations-list-en.xhtml (accessed on 18 June 2021).
11. Cohen, M.B.; Inan, U.S.; Paschal, E.W. Sensitive broadband ELF/VLF radio reception with the AWESOME instrument. *IEEE Trans. Geosci. Remote Sens.* **2010**, *48*, 3–17. [CrossRef]
12. Singh, R.; Veenadhari, B.; Cohen, M.B.; Pant, P.; Singh, A.K.; Maurya, A.K.; Vohat, P.; Inan, U.S. Initial results from AWESOME VLF receivers: Set up in low latitude Indian regions under IHY2007/UNBSSI program. *Curr. Sci.* **2010**, *98*, 398–405.
13. Chen, Y.P.; Yang, G.B.; Ni, B.B.; Zhao, Z.Y.; Gu, X.D.; Zhou, C.; Wang, F. Development of ground-based ELF/VLF receiver system in Wuhan and its first results. *Adv. Space Res.* **2016**, *57*, 1871–1880. [CrossRef]
14. Biagi, P.F.; Maggipinto, T.; Righetti, F.; Loiacono, D.; Schiavulli, L.; Ligonzo, T.; Ermini, A.; Moldovan, I.A.; Moldovan, A.S.; Buyuksarac, A.; et al. The European VLF/LF radio network to search for earthquake precursors: Setting up and natural/man-made disturbances. *Nat. Hazards Earth Syst. Sci.* **2011**, *11*, 333–341. [CrossRef]
15. Molchanov, O.; Rozhnoi, A.; Solovieva, M.; Akentieva, O.; Berthelier, J.J.; Parrot, M.; Hayakawa, M. Global diagnostics of the ionospheric perturbations related to the seismic activity using the VLF radio signals collected on the DEMETER satellite. *Nat. Hazards Earth Syst. Sci.* **2006**, *6*, 745–753. [CrossRef]
16. Muto, F.; Yoshida, M.; Horie, T.; Hayakawa, M.; Parrot, M.; Molchanov, O.A. Detection of ionospheric perturbations associated with Japanese earthquakes on the basis of reception of LF transmitter signals on the satellite DEMETER. *Nat. Hazards Earth Syst. Sci.* **2008**, *8*, 135–141. [CrossRef]
17. He, Y.; Yang, D.; Chen, H.; Qian, J.; Zhu, R.; Parrot, M. SNR changes of VLF radio signals detected onboard the DEMETER satellite and their possible relationship to the Wenchuan earthquake. *Sci. China Ser. D* **2009**, *52*, 754–763. [CrossRef]
18. Zhao, S.; Shen, X.; Zhima, Z.; Zhou, C. The very low-frequency transmitter radio wave anomalies related to the 2010 MS7.1 Yushu earthquake observed by the DEMETER satellite and the possible mechanism. *Ann. Geophys.* **2020**, *38*, 969–998. [CrossRef]
19. Zhang, X.; Zhao, S.; Song, R.; Zhai, D. The propagation features of LF radio waves at topside ionosphere and their variations possibly related to Wenchuan earthquake in 2008. *Adv. Space Res.* **2019**, *63*, 3536–3544. [CrossRef]

20. Shen, X.; Zhima, Z.; Zhao, S.; Qian, G.; Ye, Q.; Ruzhin, Y. VLF radio wave anomalies associated with the 2010 MS7.1 Yushu earthquake. *Adv. Space Res.* **2017**, *59*, 2636–2644. [CrossRef]
21. Rozhnoi, A.; Solovieva, M.; Parrot, M.; Hayakawa, M.; Biagi, P.F.; Schwingenschuh, K.; Fedun, V. VLF/LF signal studies of the ionospheric response to strong seismic activity in the Far Eastern region combining the DEMETER and ground-based observations. *J. Phys. Chem. Earth A/B/C* **2015**, *85–86*, 141–149. [CrossRef]
22. Solovieva, M.S.; Rozhnoi, A.A.; Molchanov, O.A. Variations in the parameters of VLF signals on the DEMETER satellite during the periods of seismic activity. *Geomag. Aeron.* **2009**, *49*, 532–541. [CrossRef]
23. Slominska, E.; Blecki, J.; Parrot, M.; Slominski, J. Satellite study of VLF ground-based transmitter signals during seismic activity in Honshu Island. *Phys. Chem. Earth A/B/C* **2009**, *34*, 464–473. [CrossRef]
24. Zhang, X.M. The development in seismic application research of VLF/LF radio waves. *Acta Seismol. Sin.* **2021**, *43*, 656–673. [CrossRef]
25. Yan, R.; Shen, X.; Huang, J.; Wang, Q.; Chu, W.; Liu, D.; Yang, Y.; Lu, H.; Xu, S. Examples of unusual ionospheric observations by the CSES prior to earthquakes. *Earth Planet. Phys.* **2018**, *2*, 79–90. [CrossRef]
26. Larkina, V.I.; Nalivaiko, A.V.; Gershenzon, N.I.; Gokhberg, M.B.; Liperovskii, V.A.; Shalimov, S.L. Intercosmos-19 observations of VLF emissions associated with seismic activity. *Geomagn. Aeron.* **1983**, *23*, 842–846.
27. Chmyrev, V.M.; Isaev, N.V.; Bilichenko, S.V.; Stanev, G. Observation by space-borne detectors of electric fields and hydromagnetic waves in the ionosphere over an earthquake center. *Phys. Earth Planet. Inter.* **1989**, *57*, 110–114. [CrossRef]
28. Parrot, M.; Mogilevsky, M. VLF emissions associated with earthquakes and observed in the ionosphere and magnetosphere. *Phys. Earth Planet. Inter.* **1989**, *57*, 86–99. [CrossRef]
29. Pulinets, S.A.; Legen'ka, A.D. Spatial–Temporal Characteristics of Large Scale Disturbances of Electron Density Observed in the Ionospheric F-Region before Strong earthquakes. *Cosm. Res.* **2003**, *41*, 221–230. [CrossRef]
30. Liu, Y.M.; Wang, J.S.; Xiao, Z.; Suo, Y. A Possible Mechanism of Typhoon Effects on the Ionospheric F2 layer. *Chin. J. Space Sci.* **2006**, *26*, 92–97. [CrossRef]
31. Cai, J.T.; Zhao, G.Z.; Zhan, Y.; Tang, J.; Chen, X.B. The study on ionospheric disturbances during earthquakes. *Prog. Geophys.* **2007**, *22*, 695–701.
32. Leng, X.; Ji, K.; Kuang, G. Radio Frequency Interference Detection and Localization in Sentinel-1 Images. *IEEE Trans. Geosci. Remote Sens.* **2021**, *59*, 9270–9281. [CrossRef]
33. Parrot, M. DEMETE Robservations of manmade waves that propagate in the ionosphere. *Comptes. Rendus. Phys.* **2018**, *19*, 26–35. [CrossRef]
34. Han, Y.; Yuan, J.; Feng, J.; Yang, D.; Huang, J.; Wang, Q.; Shen, X.; Zeren, Z. Automatic detection of "horizontal" electromagnetic wave disturbance in the data of EFD on ZH-1. *Prog. Geophys.* **2021**, *36*, 2303–2311.
35. Han, Y.; Yuan, J.; Feng, J.L.; Yang, D.; Huang, J.; Wang, Q.; Shen, X.; Zeren, Z. Automatic detection of horizontal electromagnetic wave disturbance in EFD data of Zh-1 based on horizontal convolution kernel. *Prog. Geophys.* **2022**, *37*, 11–18.
36. Han, Y.; Yuan, J.; Ouyang, Q.; Huang, J.; Li, Z.; Zhang, Y.; Wang, Y.; Shen, X.; Zeren, Z. Automatic Recognition of Constant-Frequency Electromagnetic Disturbances Observed by the Electric Field Detector on Board the CSES. *Atmosphere* **2023**, *14*, 290. [CrossRef]
37. Cao, J.B.; Yan, C.X.; Lu, L. Non-seismic Induced Electromagnetic Waves in the Near Earth Space. *Earthquake* **2009**, *29*, 17–25.
38. Shen, X.H.; Zong, Q.G.; Zhang, X.M. Introduction to special section on the China Seismo-Electromagnetic Satellite and initial results. *Earth Planet. Phys.* **2018**, *2*, 3–7. [CrossRef]
39. Wang, L.; Hu, Z.; Shen, X. Data processing methods and procedures of CSES satellite. *Natl. Remote Sens. Bull.* **2018**, *22*, 39–55. [CrossRef]
40. Li, Z.; Li, J.; Huang, J.; Yin, H.; Jia, J. Research on Pre-Seismic Feature Recognition of patialElectric Field Data Recorded by CSES. *Atmosphere* **2022**, *13*, 179. [CrossRef]
41. Wang, L.; Shen, X.; Zhang, Y.; Zhang, X.; Hu, Z.; Yan, R.; Yuan, S.; Zhu, X. Developing progress of China Seismo-Electromagnetic Satellite project. *Acta Seismol. Sin.* **2016**, *38*, 376–385+509.
42. Wang, X.; Yang, D.; Zhou, Z.; Cui, J.; Zhou, N.; Shen, X. Features of topside ionospheric background over China and its adjacent areas obtained by the ZH-1 satellite. *Chin. J. Geophys.* **2021**, *64*, 391–409.
43. Shen, X.; Zhang, X.; Cui, J.; Zhou, X.; Jiang, W.; Gong, L.; Li, Y.; Liu, Q. Remote sensing application in earthquake science research and geophysical fields exploration satellite mission in China. *Natl. Remote Sens. Bull.* **2018**, *22*, 1–16.
44. Zhou, B.; Cheng, B. Development and calibration of high-precision magnetometer of the China Seismo-Electromagnetic Satellite. *Natl. Remote Sens. Bull.* **2018**, *22*, 64–73.
45. Diego, P.; Huang, J.; Piersanti, M.; Badoni, D.; Zeren, Z.; Yan, R.; Rebustini, G.; Ammendola, A.; Candidi, M.; Guan, Y.-B.; et al. The Electric Field Detector on Board the China Seismo Electromagnetic Satellite-In-Orbit Results and Validation. *Instruments* **2020**, *5*, 1. [CrossRef]
46. Lu, H.; Shen, X.; Zhao, S.; Liao, L.; Lin, J.; Huang, J.; Zeren, Z.; Sun, F.; Guo, F. Typical event observation of the tri-band beacon onboard the CSES (ZH-1) satellite. *Chin. J. Radio Sci.* **2021**, *37*, 426–433. [CrossRef]
47. Liu, C.; Guan, Y.; Zheng, X.; Zhang, A.; Piero, D.; Sun, Y. The technology of space plasma in-situ measurement on the China Seismo-Electromagnetic Satellite. *Sci. China Technol. Sci.* **2019**, *62*, 829–838. [CrossRef]

48. Shen, X.; Zhang, X.; Yuan, S.; Wang, L.; Cao, J.; Huang, J.; Dai, J. The state-of-the-art of the China Seismo-Electromagnetic Satellite mission. *Sci. China Technol. Sci.* **2018**, *61*, 634–642. [CrossRef]
49. Rui, Y.; Zhe, H.; Lanwei, W.; Yibing, G.; Chao, L. Preliminary data inversion method of Langmuir probe onboard CSES. *Acta Seismol. Sin.* **2017**, *39*, 239–247.
50. Zhou, B.; Yang, Y.; Zhang, Y.; Gou, X.; Cheng, B.; Wang, J.; Li, L. Magnetic field data processing methods of the China SeismoElectromagnetic Satellite. *Earth Planet. Phys.* **2018**, *2*, 455–461. [CrossRef]
51. Ma, M.; Lei, J.; Li, C.; Zong, C.; Li, S.X.; Liu, Z.; Cui, Y. Design Optimization of Zhangheng-1 Space Electric Field Detector. *J. Vac. Sci. Technol.* **2018**, *38*, 582–589.
52. Huang, J.; Lei, J.; Li, S.; Zeren, Z.; Li, C.; Zhu, X.; Yu, W. The Electric Field Detector(EFD) onboard the ZH-1 satellite and first observational results. *Earth Planet. Phys.* **2018**, *2*, 469–478. [CrossRef]
53. Han, Y.; Yuan, J.; Huang, J.; Li, Z.; Shen, X. Automatic Detection of Electric Field VLF Electromagnetic Wave Abnormal Disturbance on Zhangheng-1 Satellite. *Atmosphere* **2022**, *13*, 807. [CrossRef]